Type-I superconductivity in the noncentrosymmetric superconductor BeAu

D. Singh,[1,2] A. D. Hillier,[2] and R. P. Singh[1,*]

[1]*Indian Institute of Science Education and Research Bhopal, Bhopal, 462066, India*

[2]*ISIS facility, STFC Rutherford Appleton Laboratory, Harwell Science and Innovation Campus, Oxfordshire OX11 0QX, United Kingdom*

(Received 15 January 2019; revised manuscript received 7 March 2019; published 11 April 2019)

The noncentrosymmetric superconductor BeAu has been investigated using magnetization, resistivity, specific heat, and muon-spin relaxation/rotation. BeAu crystallizes in a cubic FeSi-type B20 structure with a superconducting transition temperature $T_c = 3.2 \pm 0.1$ K. The low-temperature specific heat data, $C_{\rm el}$(T), indicates a weakly-coupled fully gapped BCS superconductivity with an isotropic energy gap $2\Delta(0)/k_BT_c = 3.76$, close to the BCS value of 3.52. Interestingly, type-I superconductivity is inferred from the μSR measurements, in contrast to the earlier reports of type-II superconductivity in BeAu. The Ginzburg-Landau parameter is $\kappa_{\rm GL} = 0.4 < 1/\sqrt{2}$. The frequency domain transverse-field μSR spectra, depicting the internal magnetic field probability distribution, P(B), also confirms the absence of the mixed state in BeAu. The thermodynamic critical field, H_c, is calculated to be around 259 Oe. The zero-field μSR results indicate that time-reversal symmetry is preserved and supports a spin-singlet pairing in the superconducting ground state.

DOI: 10.1103/PhysRevB.99.134509

I. INTRODUCTION

Noncentrosymmetric (NCS) superconductors (SCs) that lack an inversion symmetry in the crystal structure display a variety of unusual properties in the superconducting state [1]. In superconductors with conserved inversion symmetry, the Cooper-pair wave function is strictly determined by the parity symmetry. This means that the pair wave function consists of familiar odd and even parity labels of spin-singlet and spin-triplet Cooper pairs [2]. However, for NCS SCs the conventional Cooper pairs can no longer form. The lack of inversion symmetry in NCS SCs gives rise to an asymmetric spin-orbit coupling (ASOC) which causes the splitting of the Fermi surface [1]. This splitting allows for a mixed spin-singlet and spin-triplet pairing [1,3–5]. Mixed-parity superconductivity can lead to various exotic unconventional superconducting properties [3–7].

Evidence of unconventional superconductivity has been observed in several NCS SCs, for example: $CePt_3Si$ [8], Li_2Pt_3B [9,10], and $CeIrSi_3$ [11] exhibit lines nodes in the superconducting gap, whereas $LaNiC_2$ [12] and $(La,Y)_2C_3$ [13] show multigap superconductivity. An unusually high upper critical field, compared to the Pauli paramagnetic limiting field, has been observed in $CePt_3Si$ [14] and $Ce(Rh,Ir)Si_3$ [15,16] due to the influence of strong ASOC. Furthermore, μSR measurements have found time-reversal symmetry (TRS) breaking in $LaNiC_2$ [17], $Re_6(Ti,Zr,Hf)$ [18–20], La_7Ir_3 [21], and SrPtAs [22]. However, other systems such as: BiPd [23,24], $Nb_{0.18}Re_{0.82}$ [25], $LaMSi_3$ (M = Rh, Ir) [26,27], $LaMSi_3$ (M = Pd, Pt) [28], T_2Ga_9 (T = Rh, Ir) [29,30] appear to behave as conventional s-wave fully-gapped superconductors. These varied properties make it valuable to study additional noncentrosymmetric systems to gain a deeper understanding of their physics.

Recently, the physical properties of NCS superconductor BeAu with superconducting transition temperature $T_c = 3.3$ K were reported by Amon *et al.* [31]. The discovery of superconductivity in BeAu was first reported by B. T. Matthias in the early 1960s [32]. However, no comment was made regarding the nature of superconductivity and noncentrosymmetry in this material. BeAu undergoes a structural phase transition at $T_s = 80$ K, where it transforms from a high-temperature CsCl structure to a low-temperature FeSi structure. In the low-temperature phase (FeSi structure) Au atoms are surrounded by seven Be atoms and six Au atoms whereas in high-temperature phase (CsCl structure) Au atoms are coordinated by eight Be atoms and six Au atoms [31]. It is the cubic FeSi-type B20 structure which is noncentrosymmetric and thoroughly investigated in this work. Previously investigated superconducting properties of BeAu suggest a weakly coupled type-II superconductivity with a reported lower and upper critical field of 32 Oe and 335 Oe, respectively [31]. However, the physical properties were inadequate to define the class of superconductivity entirely. Therefore, it warrants an in-depth analysis of the superconducting state of BeAu using the muon spin rotation/relaxation (μSR) measurements. This method has been proven to be successful in determining the probability distribution of the internal fields, which subsequently can provide various types of information on the SC state.

In this paper, we have investigated the superconducting properties of BeAu using resistivity, magnetization, specific heat, and μSR measurements. The transverse-field (TF)-μSR asymmetry spectra were transformed into a probability field distribution using the maximum entropy (MaxEnt) algorithm [33] to observe the dominant field components. The TF-μSR spectra in the time domain were analyzed using a sum of Gaussian field distributions to quantify the different magnetic

*rpsingh@iiserb.ac.in

field distribution present in the sample as a function of temperature and field. Also, the zero-field (ZF)-μSR measurements were employed to search for TRS breaking phenomena in the material. Interestingly, our results suggest that BeAu can be classified as a weakly-coupled type-I superconductor with a thermodynamic critical field $H_c \simeq 259 \pm 1$ Oe in contrast with the earlier reports [31]. The Ginzburg -Landau parameter κ_{GL} obtained is around $0.4 < 1/\sqrt{2}$ again confirming type-I superconductivity in the system.

II. EXPERIMENTAL METHODS

The polycrystalline sample of BeAu was prepared by arc melting a stoichiometric mixture of elements Au (5N, Alfa Aesar) and Be (5N, Alfa Aesar) on a water-cooled copper hearth under a high purity argon gas atmosphere. The sample was melted several times sequentially without removal from the inert gas atmosphere. The mass loss (<2%) was confirmed after melting, and a small amount of beryllium was added to compensate for the Be loss. The as-cast sample was then sealed in the evacuated quartz tubes and annealed at 500 °C for 48 h.

Room temperature powder x-ray diffraction measurements were carried out on a PANalytical diffractometer (Cu $K_{\alpha 1}$ radiation, $\lambda = 1.54056$ Å). Temperature and field dependent magnetization data were collected using a Quantum Design superconducting quantum interference device (SQUID MPMS 3, Quantum Design). The measurements were performed in the temperature range of 1.8 K to 4.0 K with applied magnetic fields up to 300 Oe. The electrical resistivity and specific heat measurements were performed on a physical property measurement system (PPMS, Quantum Design, Inc.).

The μSR measurements were carried out using the MUSR spectrometer at the ISIS Neutron and Muon facility, STFC Rutherford Appleton Laboratory, United Kingdom. The powdered BeAu sample was mounted on a high-purity-silver plate using diluted GE varnish. The measurements were performed under zero-field and transverse-field conditions in the temperature range 0.1–3.5 K using a sorption He3 cryostat. A full description of the μSR technique may be found in Ref. [34]. In ZF-μSR, the contribution from the stray fields at the sample position due to neighboring instruments and the Earth's magnetic field is canceled to within ~1.0 μT by using three sets of orthogonal coils. TF-μSR measurements are performed to investigate the magnetic field distribution inside the sample. The TF-μSR data were analyzed using the MaxEnt technique to determine the probability distribution, P(B), of the internal magnetic fields. Applied fields between 50 Oe and 300 Oe were used to fully discover the superconducting phase diagram of BeAu.

III. RESULTS AND DISCUSSION

A. Structural details

Figure 1 shows the room temperature powder x-ray diffraction pattern for BeAu. The refinement shows that our sample crystallizes into a single phase of the expected noncentrosymmetric cubic FeSi-type structure with the unit cell parameter $a = 4.6684(3)$ Å. Small impurity phase is observed in the

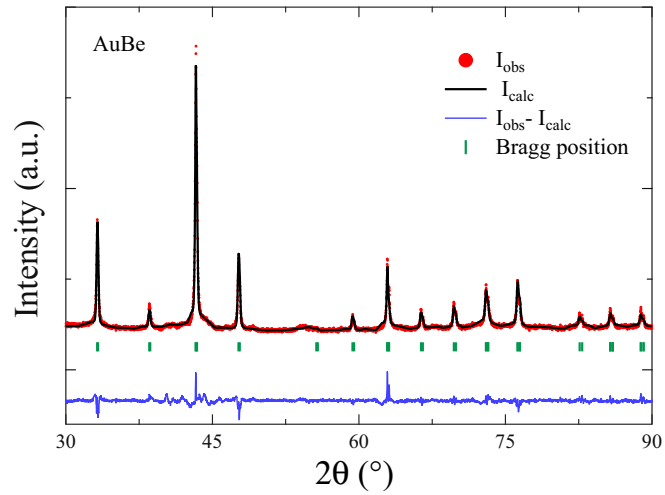

FIG. 1. The powder x-ray diffraction pattern of BeAu at room temperature. The solid black line is a Rietveld refinement to the data. The vertical tick marks indicate the calculated peak positions, and the lower graph shows the difference plot.

XRD pattern. However, no significant effect of this impurity phase is observed in the bulk and muon spectroscopy measurements. These results are in good agreement with the published literature [31].

B. Electrical resistivity

Electrical resistivity ρ versus temperature T data for BeAu was measured in zero applied magnetic field within the temperature range 1.8 K $\leqslant T \leqslant$ 300 K, as shown in Fig. 2(a). The metallic nature of the sample can be inferred from the T dependence of ρ, where resistivity decreases consistently with decreasing temperature. At $T = 300$ K, the value of the resistivity is $\rho(300\ \text{K}) \simeq 112\ \mu\Omega$ cm and the resistivity at $T = 4$ K is $\rho(4\ \text{K}) \simeq 1.35\ \mu\Omega$ cm, giving a residual resistivity ratio (RRR) ≃83. The low value of residual resistivity just above the superconducting state along with the high value of RRR reflects the good quality of our sample. The inset of Fig. 2(a) highlights the sharp drop to zero resistance below $T_{\text{conset}} = 3.25$ K, signaling the onset of superconductivity in BeAu. The zero resistivity value is reached at $T_{c0} = 3.15$ K. Transition temperature T_c, defined as the midpoint of the transition, is 3.2 ± 0.1 K, close to the previously published value [31,35]. The $\rho(T)$ measurements were performed at various applied magnetic fields between 0 Oe $\leqslant$ H $\leqslant$ 200 Oe as shown in Fig. 2(b). The application of the magnetic field suppresses T_c rapidly; at $H = 200$ Oe, T_c decreases below 1.8 K from 3.17 K at $H = 0$ Oe.

The normal-state resistivity of BeAu is analyzed using the Bloch-Grüneisen (BG) model, which describes the resistivity arising due to electron scattering from acoustic phonons. The temperature dependence of the resistivity, ρ(T), is modeled by

$$\rho(T) = \rho_0 + \rho_{\text{BG}}(T), \tag{1}$$

where ρ_0 is the temperature independent residual resistivity due to defect scattering whereas ρ_{BG} is the BG resistivity

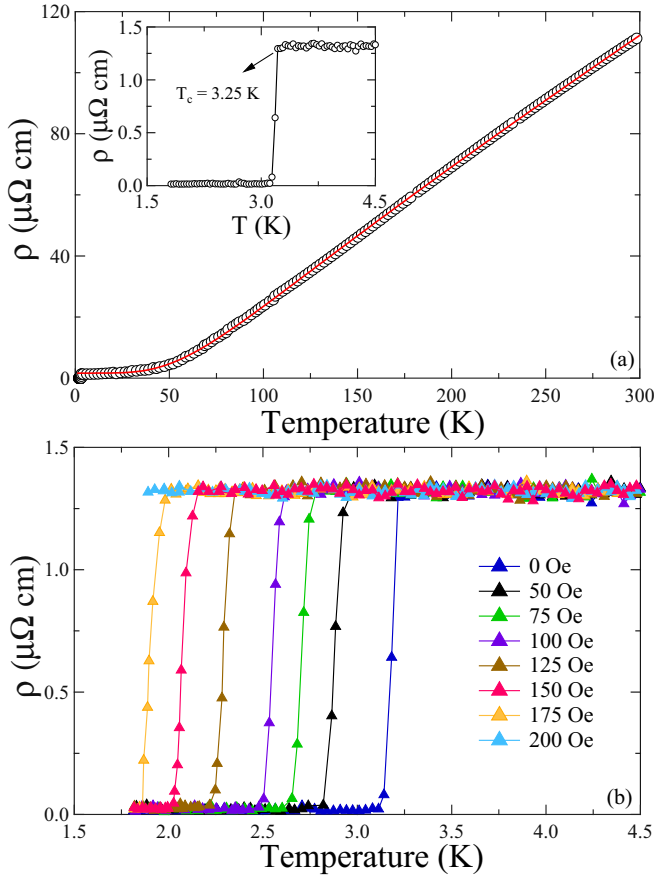

FIG. 2. (a) Temperature dependence of electrical resistivity $\rho(T)$ of BeAu for 1.8 K $\leqslant$ T $\leqslant$ 300 K measured in zero applied magnetic field. The red solid curve is a fit of $\rho(T)$ data by the Bloch-Grüneisen model. The inset shows the expanded view of $\rho(T)$ with superconductivity at $T_{\text{conset}} = 3.25$ K. (b) $\rho(T)$ of BeAu for different values of applied magnetic fields between 0 Oe $\leqslant H \leqslant$ 200 Oe.

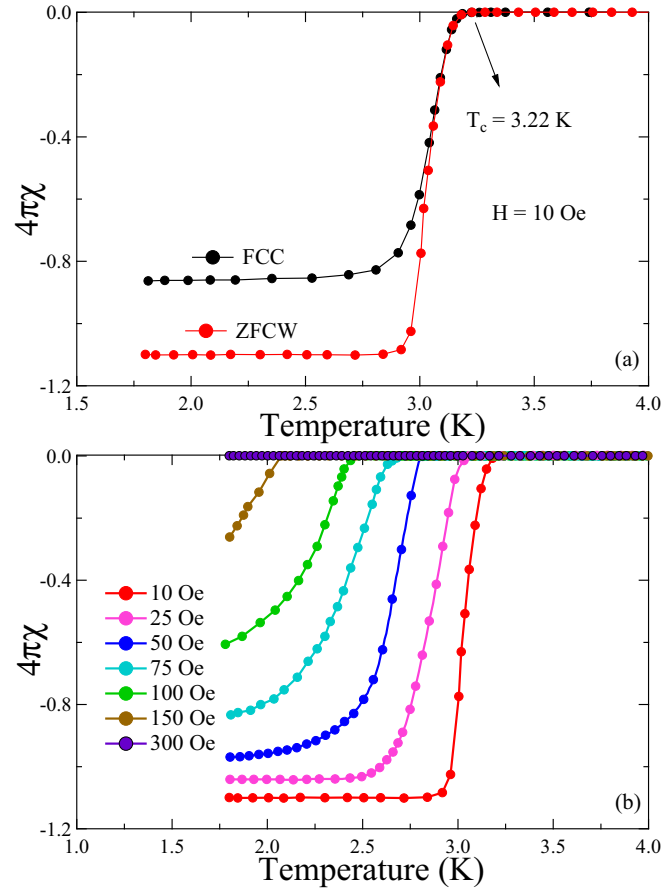

FIG. 3. (a) Temperature dependence of the dc susceptibility $\chi(T)$ in ZFCW and FCC mode shows the superconductivity at $T_{\text{conset}} = 3.22$ K. (b) The $\chi(T)$ measurements were done at different applied magnetic fields between 0 Oe $\leqslant$ H $\leqslant$ 300 Oe.

given by [36]

$$\rho_{\text{BG}}(T) = 4C\left(\frac{T}{\Theta_R}\right)^5 \int_0^{\Theta_R/T} \frac{x^5}{(e^x-1)(1-e^{-x})}dx, \quad (2)$$

where Θ_R is the Debye temperature obtained from resistivity measurements, while C is a material dependent prefactor [37]. The best fit for the above data using the BG model is shown by the solid red curve in Fig. 2(a) and yields a Debye temperature $\Theta_R = (345 \pm 2)$ K, C = (136 ± 15) $\mu\Omega$ cm and residual resistivity $\rho_0 = (1.36 \pm 0.05)$ $\mu\Omega$ cm. The value of the Debye temperature Θ_R is close to that extracted later from the specific heat measurements.

The mean free path l can be calculated using the Fermi velocity v_F and the scattering time τ using the relation $l = v_F\tau$. Based on the Drude model, v_F is given by $\hbar k_F/\text{m}^*$ and scattering time $\tau^{-1} = \text{ne}^2\rho_0/\text{m}^*$, where m* is the effective mass, k_F is the Fermi vector, and n is the electron carrier density. As already shown in Ref. [31], the electron density for BeAu is $n = 4/V = 3.93 \times 10^{28}$ m^{-3} for $V = 101.746$ Å^3. Assuming a spherical Fermi surface, we can use the above value of n to estimate the Fermi wave vector $k_F = (3\text{n}\pi^2)^{1/3} = 1.05$ Å^{-1}. The effective mass m* is estimated to be 2.8 m_e, using the values for γ_n (from specific heat measurement), k_F, and n [31]. From the calculated values of m*, n, k_F, and ρ_0, we determined the Fermi velocity $v_F = 4.34 \times 10^5$ m/s and mean free path $l = 808.2$ Å.

C. Magnetization

Superconductivity in BeAu was further confirmed by dc susceptibility (χ) measurements taken in zero-field cooled warming (ZFCW) and field-cooled cooling (FCC) mode as shown in Fig. 3(a). The data measured in an applied field of 10 Oe demonstrates the onset of a sharp superconducting transition at T$_{\text{conset}} = 3.2 \pm 0.1$ K. The value of Meissner fraction $4\pi\chi$ exceeds 100% due to the demagnetization effects [38]. However, it indicates a complete flux expulsion in the compound. The plot for $\chi(T)$ measurements in several applied magnetic fields up to 300 Oe is shown in Fig. 3(b). The application of the applied magnetic field strongly suppresses the transition temperature: T_{conset} becomes smaller than 1.8 K for $H > 150$ Oe. The magnetization measurement (M) as a function of field (H) at $T = 1.8$ K is shown in Fig. 4(a). The isothermal magnetization curve follows a near typical type-I superconducting behavior. Decreasing the applied magnetic field from $H = 300$ Oe exhibit a partial re-entrance of diamagnetization as magnetic flux is expelled

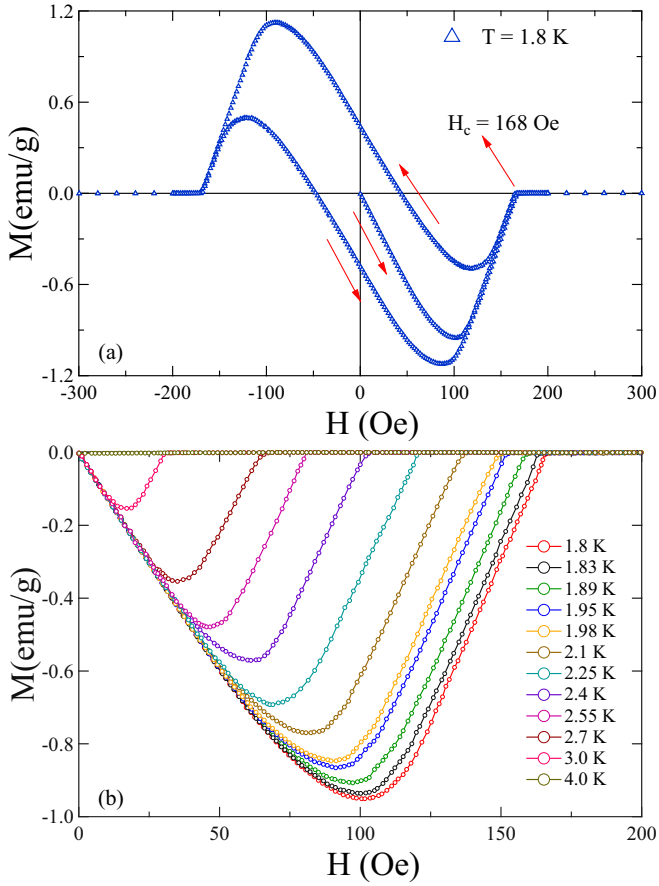

FIG. 4. (a) Magnetization as a function of applied field measured at 1.8 K. (b) Magnetic isotherms, M(H), for the temperature range 1.8 K $\leqslant T \leqslant$ 4.0 K.

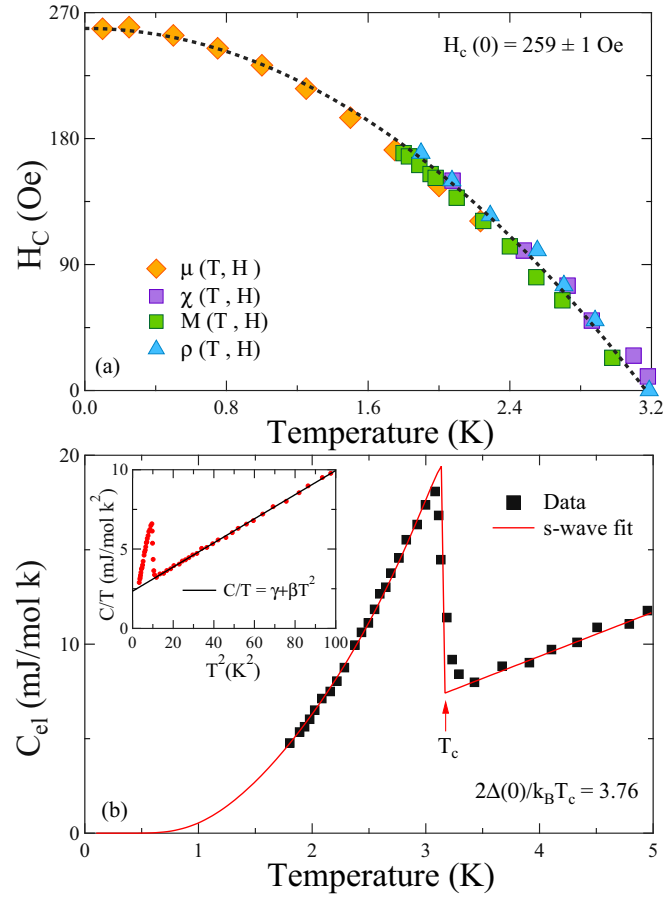

FIG. 5. (a) Thermodynamic critical field H_c as a function of temperature obtained from $\rho(T)$, M(H), $\chi(T)$, and muon experimental data. The solid line represents the fit using the function $H_c(T) = H_c(0)[1-(T/T_c)^2]$. (b) Zero-field electronic specific heat data, $C_{\rm el}$, as a function of temperature T. The solid red curve represents the fully gapped superconductivity with $2\Delta(0)/k_B\ T_c = 3.76$. The inset shows the C/T vs T^2 data, where it's fitted using the relation $C/T = \gamma + \beta {\rm T}^2$.

from the system. Such a kind of magnetization data has been observed in other type-I superconducting materials such as: $LaRhSi_3$ [27], $LaMSi_3$ (M= Pd,Pt) [28], Ir_2Ga_9 [29]. The absence of the typical step transition at the critical field could be due to the demagnetization factor which often broadens the transition. Figure 4(b) displays the field dependence of the magnetization, M(H), which is performed at different temperatures from 1.8 K $\leqslant T \leqslant$ 4 K. It should be noted that the high-quality sample for a type-I superconductor gives a sharp transition in magnetic isotherms. Compared to the data presented in Fig. 4(b), the magnetic isotherms in Ref. [31] are rather rounded on the high-field side. This could be due to the different quality of samples used in the respective measurements. The value for the thermodynamic critical field $H_c(T)$ is defined as the field at which the system goes from the superconducting state to the normal state. For example: $H_c =$ 168 Oe at $T = 1.8$ K [see Fig. 4(a)]. The resulting values of H_c determined in this manner for different temperatures are summarized in Fig. 5(a) together with the values determined from the $\rho(T)$, $\chi(T)$, and muon data. The $H_c(T)$ can be described by the conventional relation

$$H_c = H_c(0)\left[1-\left(\frac{T}{T_c}\right)^2\right], \tag{3}$$

where T_c is the superconducting transition temperature and $H_c(0)$ is the critical field value for $T = 0$. Dotted black curve shows the best fit for the data which yields $H_c(0) = 259 \pm 1$ Oe.

D. Specific heat

Figure 5(b) shows the specific heat data of BeAu measured in zero applied magnetic field. The sharp jump around $T_c \simeq$ 3.17 K confirms the intrinsic nature of superconductivity in this compound. The plot C/T versus T^2 is shown in the inset of Fig. 5(b) and shows, in the normal state, the data is best represented by $C/T = \gamma_n + \beta T^2$, where γ_n is the Sommerfeld coefficient and the second term β is the contribution from lattice. The solid black curve in the inset represents the fit to the data, yielding $\gamma_n = 2.35 \pm 0.02$ mJ mol^{-1} K^{-2} and $\beta = 0.076 \pm 0.003$ mJ mol^{-1} K^{-4}. The value for γ_n was used to determine the density of states at the Fermi level $D_c(E_{\rm F})$ using the relation $\gamma_n = (\pi^2 k_B^2 D_c(E_{\rm F}))/3$, where $E_{\rm F}$ is the Fermi energy. For $\gamma_n = 2.35 \pm 0.02$ mJ mol^{-1} K^{-2}, it yields $D_c(E_{\rm F}) \simeq 1.0 \pm 0.1$ states eV^{-1} f.u.$^{-1}$. The Debye temperature is given by $\theta_D = (12\pi^4 RN/5\beta)^{1/3}$, where using

$R = 8.314$ J mol^{-1} K^{-1} and $N = 2$, which yields $\theta_D = 370 \pm 5$ K. The value of $\theta_D = 370$ K can be used to calculate the electron-phonon coupling constant $\lambda_{e\text{-ph}}$ using the McMillan formula [39],

$$\lambda_{e\text{-ph}} = \frac{1.04 + \mu^* \ln(\theta_D/1.45T_c)}{(1 - 0.62\mu^*)\ln(\theta_D/1.45T_c) - 1.04}, \quad (4)$$

where μ^* represents the repulsive screened Coulomb potential, usually given by $\mu^* = 0.13$. With $T_c = 3.17$ K and $\theta_D = 370$ K, we obtained $\lambda_{e\text{-ph}} \simeq 0.54$, which is similar to other weakly coupled NCS superconductors [25,27,28,40,41]. The bare-band effective mass m^*_{band} can be related to m^*, which contains enhancements from the many-body electron phonon interactions $m^* = m^*_{band}(1 + \lambda_{e\text{-ph}})$ [36]. Using $\lambda_{e\text{-ph}} = 0.54$ and assuming $m^*_{band} = m_e$ gives $m^* = 1.54\ m_e$.

The electronic contribution (C_{el}) to the specific heat determined by subtracting the phononic contribution from the measured specific heat data, i.e., $C_{el} = C - \beta T^3$, shown in the main panel of Fig. 5(b). The value for the specific heat jump is $\frac{\Delta C}{\gamma_n T_c} \simeq 1.51$, which is close to the value for a BCS isotropic gap superconductor (=1.43). This indicates weakly-coupled superconductivity in BeAu, consistent with the $\lambda_{e\text{-ph}}$ value obtained above. The temperature dependence of the specific heat data in the superconducting state can best be described by the BCS expression for the normalized entropy S written as

$$\frac{S}{\gamma_n T_c} = -\frac{6}{\pi^2}\left(\frac{\Delta(0)}{k_B T_c}\right)\int_0^\infty [f\ln(f) + (1-f)\ln(1-f)]dy, \quad (5)$$

where $f(\xi) = [\exp(E(\xi)/k_BT)+1]^{-1}$ is the Fermi function, $E(\xi) = \sqrt{\xi^2 + \Delta^2(t)}$, where ξ is the energy of normal electrons measured relative to the Fermi energy, $y = \xi/\Delta(0)$, $t = T/T_c$, and $\Delta(t) = \tanh[1.82(1.018((1/t) - 1))^{0.51}]$ is the BCS approximation for the temperature dependence of the energy gap. The normalized electronic specific heat is calculated by

$$\frac{C_{el}}{\gamma_n T_c} = t\frac{d(S/\gamma_n T_c)}{dt}. \quad (6)$$

Fitting the low temperature specific heat data using the above model as shown by the solid red line in Fig. 5(b) gives $\Delta(0)/k_BT_c = 1.82 \pm 0.2$. This value is consistent with the value for a BCS superconductor $\alpha_{BCS} = 1.764$ in the weak coupling limit. Therefore, good agreement between the measured data (black symbols) and the BCS fit (solid red line), confirms an isotropic fully gapped BCS superconductivity in BeAu.

E. Muon spin relaxation and rotation

The time evolution of muon spin relaxation in zero field is shown in Fig. 6 for temperatures both above $T = 3.5$ K and below $T = 0.1$ K the transition temperature T_c. The ZF-μSR spectra are well fitted with the following function:

$$G(t) = A_1 \exp(-\lambda t) G_{KT}(t) + A_{BG}, \quad (7)$$

where A_1 is the initial asymmetry, λ is the electronic relaxation rate, and A_{BG} is the time-independent background

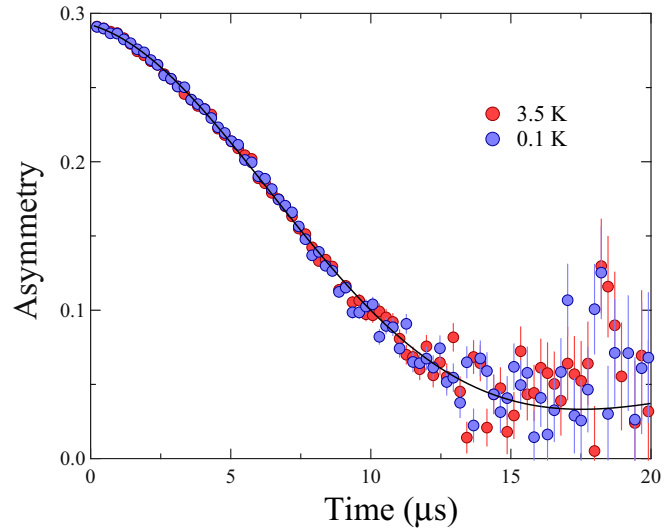

FIG. 6. Zero-field μSR spectra collected below (0.1 K) and above (3.5 K) the superconducting transition temperature. The solid lines are the fits to Guassian Kubo-Toyabe (KT) function given in Eq. (7).

contribution. The $G_{KT}(t)$ function is the Gaussian Kubo-Toyabe function given by

$$G_{KT}(t) = \frac{1}{3} + \frac{2}{3}(1 - \sigma^2_{ZF}t^2)\exp\left(-\frac{\sigma^2_{ZF}t^2}{2}\right), \quad (8)$$

where σ_{ZF}/γ_μ is the local field distribution width, $\gamma_\mu/2\pi = 135.5$ MHz/T being the muon gyromagnetic ratio. In systems where the superconducting state breaks time-reversal symmetry, spontaneous magnetic moments arise below T_c, and an increase may be observed in either σ_{ZF} or λ. It is evident from the ZF-μSR spectra that there is no noticeable change in the relaxation rates at either side of the superconducting transition. This indicates that the time-reversal symmetry is preserved in the SC phase within the experimental accuracy.

The transverse-field μSR data were collected after cooling the sample in an applied field from the normal state to the superconducting state. The TF-μSR precession signals were obtained in different applied magnetic fields up to 300 Oe. Figure 7 show the typical MaxEnt results of the magnetic field distribution, extracted from the TF-μSR time spectra, in the (a) Meissner, (c) intermediate, and (e) normal state. Figures 7(b), 7(d) and 7(f) show the TF-μSR time spectra for the corresponding states. At $H_{app} = 50$ Oe and $T = 0.1$ K, BeAu is in the Meissner state. This state is well reflected in the MaxEnt results shown in the inset of Fig. 7(a). The peak near $B_{int} \simeq 3$ G corresponds to the dominant contribution of Be/Au nuclear moments. In the main panel of Fig. 7(a), the second peak around $B = 50$ G is a background signal arising mainly due to the muons stopping in the silver sample holder. The absence of any additional peak implies that the magnetic field is completely expelled from the body of the superconductor. Figure 7(b) shows the TF-μSR spectra in the Meissner state ($H_{app} = 50$ Oe, $T = 0.1$ K) where the weak decay suggests the Kubo-Toyabe behavior associated with the nuclear moments. Interestingly, there is a considerable reduction in the initial asymmetry of the

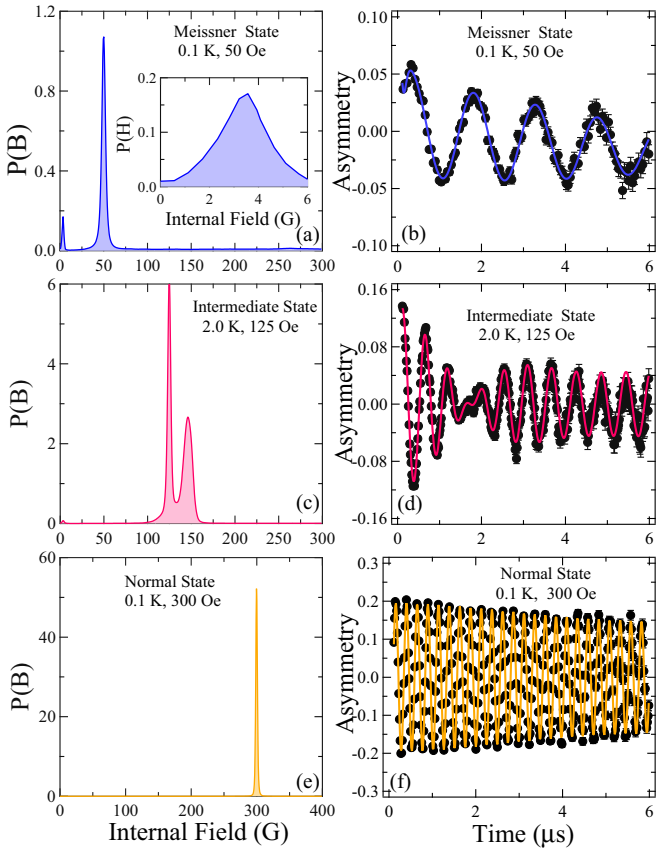

FIG. 7. Field distributions and TF-μSR signals. Field distribution of the local field probed by the muons, P(B), obtained by MaxEnt transformation of the TF-μSR time spectra at different temperatures and applied field. The figure illustrates typical signal observed in the (a) Meissner, (c) intermediate state, and (e) normal state. (b), (d), and (f) show the TF-μSR time spectra for the corresponding states. The solid lines are fits to the data using a fit function, described in Eq. (9).

spectra. The loss of initial asymmetry as observed in our TF-μSR spectra of BeAu is similar to that observed in type-I superconductors $LaRhSi_3$ [27], LaNiSn [42], and the recently published BeAu [35]. The missing asymmetry behavior is due to the detectors in the TF geometry unable to detect the positrons emitted in the muon spin polarization direction when the sample is in the Meissner state [35]. At the higher applied field or temperature near T_c the initial asymmetry recovers to its full maximum value.

The TF-μSR spectra at $H_{app} = 125$ Oe field and $T = 2.0$ K shown in Fig. 7(d). We analyze the spectra using the following function:

$$G_z(t) = G(t) + \sum_{i=1}^{N} A_i \exp\left(-\frac{1}{2}\sigma_i^2 t^2\right) \cos(\gamma_\mu B_i t + \phi), \tag{9}$$

where G(t) is Eq. (7), A_i is the initial asymmetry, σ_i is the Gaussian relaxation rate, $\gamma_\mu/2\pi = 135.5$ MHz/T is the muon gyromagnetic ratio, ϕ is the common phase offset, and B_i is the first moment for the ith component of the field distribution. We found that the asymmetry spectra can best be described by two oscillating functions ($N = 2$). In these fits, the $i = 1$ depolarization component was fixed to $\sigma_1 = 0$, which corresponds to a background term arising from those muons stopping in the silver sample holder as they do not appreciably depolarize over the time scale of the experiment. From these fits, we obtain the value of the internal magnetic fields 125 G and 146 G. The former value of the internal field is the same as the applied field (from the silver holder), while the latter value can be taken as an estimate of the critical field (H_c) coming from the intermediate state of a type-I superconductor. The intermediate state of a type-I superconductor is induced by the nonzero demagnetization effects. Demagnetization effects cause some part of the superconducting sample to experience a field greater than the applied magnetic field. In such a situation, a stable coexistence of the flux-free regions (superconducting regions) and the regions with internal field $\simeq H_c$ (normal regions) arises even if the applied magnetic field, H_{app}, is considerably less than the critical field H_c. Muons implanted in these normal regions of the intermediate state will precess at a frequency corresponding to the field equal to H_c, whereas the muons landing in the superconducting regions will be stationary and only be affected by the nuclear moments. The muons stopping in the silver holder will precess with the applied magnetic field. In the MaxEnt data shown in Fig. 7(c), the intermediate state is well demonstrated by the two sharp peaks. For a type-II superconductor in the mixed state, we expect a component at a lower field value than the applied field due to the establishment of the flux-line lattice (FLL). This is clearly absent for our sample. On the contrary, we observe a peak near $B_{int} = 146$ G $> H_{app}$, suggesting the intermediate state in BeAu. This is strong evidence for bulk type-I superconductivity in the compound. Indeed, similar results on BeAu [35] are reported by James *et al.* using the μSR and magnetometry measurements which again confirms the above conclusion.

In the magnetic field of $H_{app} = 300$ Oe and $T = 0.1$ K, BeAu returns to the normal state. Here, the field penetrates the bulk of the sample completely, and we see an almost homogeneous field distribution in the TF-μSR time spectra as displayed in Fig. 7(f). Accordingly, a single sharp peak is observed at $B_{int} = 300$ G in the maximum entropy spectra in Fig. 7(e).

Figure 8(a) shows the internal field distribution, P(B), obtained by MaxEnt transformation at different applied fields between 50 Oe $\leqslant H \leqslant$ 250 Oe at constant temperature $T =$ 0.1 K. The internal field distribution at $T = 0.1$ K clearly demonstrates the change from the Meissner state ($H_{app} =$ 50 Oe) to the intermediate state ($H_{app} = 150$ Oe) to the normal state ($H_{app} = 250$ Oe) with increasing magnetic field. At the intermediate state for $H_{app} > 50$ Oe, P(B) shows an additional peak at $H_c > H_{app}$ corresponding to the normal regions in the sample. Notably, there is not a significant change in the H_c peak position with the increase in the applied magnetic field again confirming the type-I behavior in BeAu. For a type-II superconductor in the mixed state the internal field is always less than the applied field and changes as a function of the applied field. It is noteworthy here that for $H_{app} \geqslant 50$ Oe we observed a systematic decrease in the peak near $B_{int} \sim 3$ G [see inset Fig. 8(a)]. This can be understood from the fact that in the low applied field (50 Oe) the sample is in the Meissner

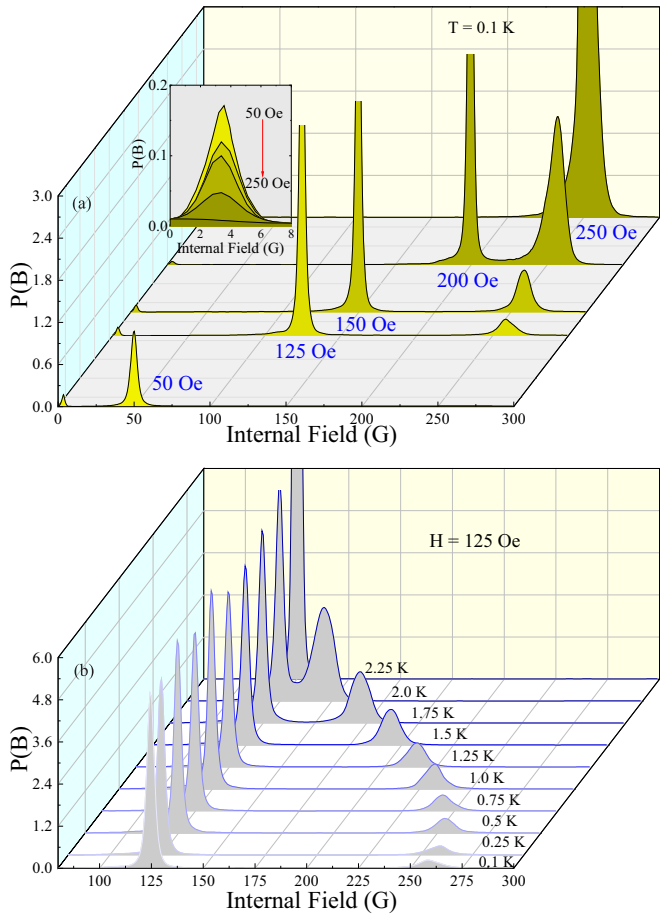

FIG. 8. (a) Field distribution of the internal field probed by the muons, P(B), obtained by MaxEnt transformation at different fields between 50 Oe $\leqslant H \leqslant$ 250 Oe at $T = 0.1$ K and (b) between 0.1 K $\leqslant T \leqslant$ 2.25 K at applied field $H = 125$ Oe.

state, depicted by the highest peak in the inset graph. As the applied field is increased, the system goes to the intermediate state which consequently decreases the Meissner volume fraction. Since the P(B) peak near the low-field region arises from the Meissner state, it is understandable that it decreases with the increase in the applied field. At $H_{\rm app} = 250$ Oe the system goes to the normal state which is apparent from the presence of only one peak in the P(B) graph.

The maximum entropy spectra for TF-μSR in a range of temperatures between 0.1 K $\leqslant T \leqslant$ 2.25 K are shown in Fig. 8(b). The sample was cooled in an applied field of $H_{\rm app} =$ 125 Oe, and the measurements were made while warming. At $T = 0.1$ K, two different peaks appear in the P(B) spectra at $B_{\rm int} \simeq H_{\rm app} \simeq 125$ G and $B_{\rm int} \simeq H_c \simeq 256$ G, reminiscent of the intermediate state in a type-I superconductor. A peak also appears in the low-field region due to the superconducting regions in the sample. Interestingly, as the temperature is increased the peak position for H_c moves closer to $H_{\rm app}$ with a subsequent increase in the magnitude. The observed behavior is due to an increase in the volume of the normal core regions in the intermediate state. Thus, we can deduce the H-T phase diagram from the peak position of the critical field H_c. The obtained phase diagram is shown in Fig. 5(a) and is in good agreement with those obtained from the other measurement techniques. The critical field $H_c(0)$ is 259 ± 1 Oe obtained after fitting Eq. (3).

F. Uemura plot

We now investigate the superconducting parameters of BeAu. The London penetration depth is given by the relation $\lambda_L = (m^*/\mu_0 n e^2)^{1/2}$. Putting in the values $m^* = 2.8 m_e$ and $n = 3.93 \times 10^{28}$ m^{-3}, yields $\lambda_L \simeq 450$ Å. The BCS coherence length can be evaluated using the expression $\xi_0 = (\frac{0.18\hbar v_F}{k_B T_c}) \simeq 1883$ Å. As ξ_0 is larger than the calculated mean free path $l(808.2$ Å), $l/\xi_0 \simeq 0.43 \ll 1$, indicating that the superconductivity in BeAu is in the dirty limit. In the dirty limit, the Ginzburg-Landau (GL) parameter $\kappa_{\rm GL} = 0.715\, \lambda_L(0)/l$ [43], which gives $\kappa_{\rm GL} \simeq 0.4$. $\kappa_{\rm GL}$ is smaller than the value $1/\sqrt{2} \simeq 0.707$ separating type-I and type-II superconductivity, suggesting that BeAu is a type-I superconductor. Further using the relation $\kappa_{\rm GL} = 7.49 \times 10^3\ \rho_0 \sqrt{\gamma_{nV}}$, with ρ_0 in Ω cm and γ_{nV} in units erg/cm^3 K^2, we obtained $\kappa_{\rm GL} =$ 0.4, consistent with the value obtained above. The effective magnetic penetration depth $\lambda_{\rm eff}$ is equal to 821 Å, which is calculated using the relation $\lambda_{\rm eff} = \lambda_L \sqrt{1 + \xi_0/l}$. In addition, the Ginzburg-Landau coherence length $\xi(0)$ is determined from the relation $\kappa_{\rm GL} = \lambda_{\rm eff}/\xi(0)$, which gives $\xi(0) = 2052$ for $\kappa_{\rm GL} = 0.4$.

According to Uemura *et al.* [44–46] superconductors can be conveniently classified according to their $\frac{T_c}{T_F}$ ratio. It was shown that for the unconventional superconductors such as

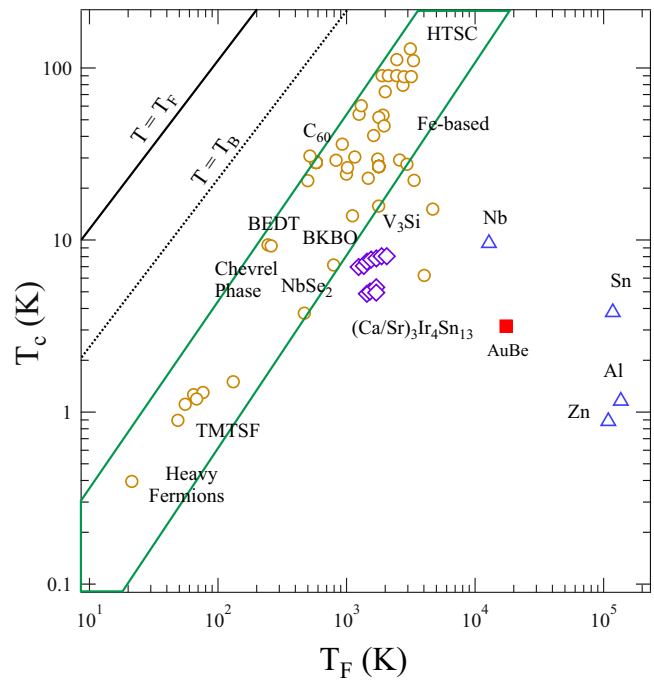

FIG. 9. The Uemura plot showing the superconducting transition temperature T_c vs the Fermi temperature T_F, where BeAu is shown as a solid red square marker well outside the range of band of unconventional superconductors. The region displayed by the solid green lines represents the band of unconventionality obtained from Refs. [44–46].

TABLE I. Normal and superconducting properties of noncentrosymmetric superconductor BeAu.

Parameter	Unit	Value
T_c	K	3.2
γ_n	mJ mol^{-1} K^{-1}	2.35
θ_D	K	370
$\Delta C_{\rm el}/\gamma_n T_c$		1.51
H_c	Oe	259
$\kappa_{\rm GL}$		0.4
$\xi(0)$	Å	2052
ξ_0	Å	1883
l	Å	808.2
λ_L	Å	450
$\lambda_{\rm eff}$	Å	821
$T_{\rm F}$	K	17450
$T_c/T_{\rm F}$		0.00018

heavy-fermion, high-T_c, organic superconductors and iron-based superconductors this ratio falls in the range $0.01 \leqslant \frac{T_c}{T_F} \leqslant 0.1$. In Fig. 9, the region between the solid green lines represents the band of unconventional superconductors. For a 3D system, the Fermi temperature T_F is given by the relation

$$k_B T_F = \frac{\hbar^2 k_F^2}{2m^*}, \tag{10}$$

where k_F is the Fermi vector. Using the estimated value of k_F for BeAu in Eq. (10), it yields $T_F = 17\,450$ K, giving $\frac{T_c}{T_F} \simeq 0.00018$. BeAu is located well outside the range of unconventional superconductors and close to the vicinity of elemental superconductors which are type-I BCS superconductors as shown by a solid red marker in Fig. 9. This suggests conventional mechanism of superconductivity in BeAu (Table I).

IV. CONCLUSIONS

To summarize, we have investigated the superconducting properties of cubic noncentrosymmetric superconductor BeAu using magnetization, resistivity, specific heat, and μSR measurements. BeAu undergoes a superconducting transition at $T_c = 3.2$ K. The specific heat data measured in zero applied field shows BCS superconductivity in the weak-coupling regime. The magnetization measurements along with the calculated superconducting parameters suggest type-I superconductivity in this compound, in contrast to the earlier reports which showed type-II superconductivity. The thermodynamic critical field $H_c \simeq 259$ Oe and the GL parameter $\kappa_{\rm GL}$ is $0.4 \ll 1/\sqrt{2}$, again confirming type-I superconductivity. The microscopic study of superconductivity in BeAu was done by μSR measurements. The TF-μSR data was transformed into the probability distribution of internal fields, P(B), using the MaxEnt algorithm. The field components obtained don't show any signs of mixed state to suggest type-II superconductivity in BeAu. In a type-II superconductor in the mixed state, the peak corresponding to the applied field broadens, and an additional shoulder in the distribution is observed at lower fields due to flux line lattice. However, this feature was not seen for any temperature or field. An internal field at a higher field H_c than the applied field $H_{\rm app}$ is found which is strong evidence for bulk type-I superconductivity in the compound. Furthermore, the ZF-μSR analysis indicates that the time-reversal symmetry is preserved in the superconducting state. Theoretically, the spin-triplet pairing or the admix pairing state is allowed in NCS superconductors. However, the lack of inversion symmetry in BeAu doesn't seem to affect the superconducting ground state, where the superconductivity turned out to be BCS-like with a singlet pairing. This raises an essential question of what stimulates the anomalous superconducting state in an NCS system: Is it just the degree of crystal structure deformation which strengthens the ASOC, or are some other parameters also involved? Notably, the size of splitting due to NCS structure is very important since if the splitting size is small the overall effect of no inversion symmetry is negated. Therefore, further studies such as photoemission spectroscopy would be beneficial to understand the superconducting gap structure in BeAu.

ACKNOWLEDGMENTS

R.P.S. acknowledges Science and Engineering Research Board, Government of India for the Ramanujan Fellowship through Grant No. SR/S2/RJN-83/2012. We thank Newton Bhabha funding and ISIS, STFC, UK, for the muon beam time to conduct the μSR experiments [47].

[1] E. Bauer and M. Sigrist, *Non-centrosymmetric Superconductors:Introduction and Overview*, Vol. 847 (Springer Science & Business Media, Berlin, 2012).
[2] P. W. Anderson, Phys. Rev. B **30**, 4000 (1984).
[3] V. M. Edelstein, Phys. Rev. Lett. **75**, 2004 (1995).
[4] V. M. Edelstein, Zh. Ekep. Teor. Fiz. **95**, 2151 (1989) [Sov. Phys. JETP 68, 1244 (1989)].
[5] L. P. Gor'kov and E. I. Rashba, Phys. Rev. Lett. **87**, 037004 (2001).
[6] S. K. Yip, Phys. Rev. B **65**, 144508 (2002).
[7] S. Fujimoto, J. Phys. Soc. Jpn. **76**, 051008 (2007).
[8] I. Bonalde, W. Brämer-Escamilla, and E. Bauer, Phys. Rev. Lett. **94**, 207002 (2005).
[9] H. Q. Yuan, D. F. Agterberg, N. Hayashi, P. Badica, D. Vandervelde, K. Togano, M. Sigrist, and M. B. Salamon, Phys. Rev. Lett. **97**, 017006 (2006).
[10] M. Nishiyama, Y. Inada, and G.-Q. Zheng, Phys. Rev. Lett. **98**, 047002 (2007).
[11] H. Mukuda, T. Fujii, T. Ohara, A. Harada, M. Yashima, Y. Kitaoka, Y. Okuda, R. Settai, and Y. Onuki, Phys. Rev. Lett. **100**, 107003 (2008).
[12] J. Chen, L. Jiao, J. L. Zhang, Y. Chen, L. Yang, M. Nicklas, F. Steglich, and H. Q. Yuan, New J. Phys. **15**, 053005 (2013).
[13] S. Kuroiwa, Y. Saura, J. Akimitsu, M. Hiraishi, M. Miyazaki, K. H. Satoh, S. Takeshita, and R. Kadono, Phys. Rev. Lett. **100**, 097002 (2008).

[14] E. Bauer, G. Hilscher, H. Michor, C. Paul, E. W. Scheidt, A. Gribanov, Y. Seropegin, H. Noël, M. Sigrist, and P. Rogl, Phys. Rev. Lett. **92**, 027003 (2004).
[15] N. Kimura, K. Ito, H. Aoki, S. Uji, and T. Terashima, Phys. Rev. Lett. **98**, 197001 (2007).
[16] I. Sugitani, Y. Okuda, H. Shishido, T. Yamada, A. Thamizhavel, E. Yamamoto, T. D. Matsuda, Y. Haga, T. Takeuchi, R. Settai, and Y. Onuki, J. Phys. Soc. Jpn. **75**, 043703 (2006).
[17] A. D. Hillier, J. Quintanilla, and R. Cywinski, Phys. Rev. Lett. **102**, 117007 (2009).
[18] D. Singh, S. K. P., J. A. T. Barker, D. M. Paul, A. D. Hillier, and R. P. Singh, Phys. Rev. B **97**, 100505(R) (2018).
[19] R. P. Singh, A. D. Hillier, B. Mazidian, J. Quintanilla, J. F. Annett, D. M. Paul, G. Balakrishnan, and M. R. Lees, Phys. Rev. Lett. **112**, 107002 (2014).
[20] D. Singh, J. A. T. Barker, A. Thamizhavel, D. M. Paul, A. D. Hillier, and R. P. Singh, Phys. Rev. B **96**, 180501(R) (2017).
[21] J. A. T. Barker, D. Singh, A. Thamizhavel, A. D. Hillier, M. R. Lees, G. Balakrishnan, D. M. Paul, and R. P. Singh, Phys. Rev. Lett. **115**, 267001 (2015).
[22] P. K. Biswas, H. Luetkens, T. Neupert, T. Sturzer, C. Baines, G. Pascua, A. P. Schnyder, M. H. Fischer, J. Goryo, M. R. Lees, H. Maeter, F. Bruckner, H. H. Klauss, M. Nicklas, P. J. Baker, A. D. Hillier, M. Sigrist, A. Amato, and D. Johrendt, Phys. Rev. B **87**, 180503(R) (2013).
[23] K. Matano, S. Maeda, H. Sawaoka, Y. Muro, T. Takabatake, B. Joshi, S. Ramakrishnan, K. Kawashima, J. Akimitsu, and G.-Q. Zheng, J. Phys. Soc. Jpn. **82**, 084711 (2013).
[24] X. B. Yan, Y. Xu, L. P. He, J. K. Dong, H. Cho, D. C. Peets, J.-G. Park, and S. Y. Li, Supercond. Sci. Technol. **29**, 065001 (2016).
[25] A. B. Karki, Y. M. Xiong, N. Haldolaarachchige, S. Stadler, I. Vekhter, P. W. Adams, D. P. Young, W. A. Phelan, and J. Y. Chan, Phys. Rev. B **83**, 144525 (2011).
[26] V. K. Anand, D. Britz, A. Bhattacharyya, D. T. Adroja, A. D. Hillier, A. M. Strydom, W. Kockelmann, B. D. Rainford, and K. A. McEwen, Phys. Rev. B **90**, 014513 (2014).
[27] V. K. Anand, A. D. Hillier, D. T. Adroja, A. M. Strydom, H. Michor, K. A. McEwen, and B. D. Rainford, Phys. Rev. B **83**, 064522 (2011).
[28] M. Smidman, A. D. Hillier, D. T. Adroja, M. R. Lees, V. K. Anand, R. P. Singh, R. I. Smith, D. M. Paul, and G. Balakrishnan, Phys. Rev. B **89**, 094509 (2014).
[29] K. Wakui, S. Akutagawa, N. Kase, K. Kawashima, T. Muranaka, Y. Iwahori, J. Abe, and J. Akimitsu, J. Phys. Soc. Jpn. **78**, 034710 (2009).
[30] T. Shibayama, M. Nohara, H. A. Katori, Y. Okamoto, Z. Hiroi, and H. Takagi, J. Phys. Soc. Jpn. **76**, 073708 (2007).
[31] A. Amon, E. Svanidze, R. Cardoso-Gil, M. N. Wilson, H. Rosner, M. Bobnar, W. Schnelle, J. W. Lynn, R. Gumeniuk, C. Hennig, G. M. Luke, H. Borrmann, A. Leithe-Jasper, and Yu. Grin, Phys. Rev. B **97**, 014501 (2018).
[32] B. T. Matthias, J. Phys. Chem. Solids **10**, 342 (1959).
[33] B. D. Rainford and G. J. Daniell, Hyperfine Interact. **87**, 1129 (1994).
[34] S. L. Lee, S. H. Kilcoyne, and R. Cywinski, *Muon Science: Muons in Physics, Chemistry and Materials* (SUSSP Publications and IOP Publishing, Bristol, 1999).
[35] J. Beare, M. Nugent, M. N. Wilson, Y. Cai, T. J. S. Munsie, A. Amon, A. Leithe-Jasper, Z. Gong, S. L. Guo, Z. Guguchia, Y. Grin, Y. J. Uemura, E. Svanidze, and G. M. Luke, Phys. Rev. B **99**, 134510 (2019).
[36] G. Grimvall, *The Electron-Phonon Interaction in Metals* (North Holland, Amsterdam, 1981).
[37] A. Bid, A. Bora, and A. K. Raychaudhuri, Phys. Rev. B **74**, 035426 (2006).
[38] A. Aharoni, J. Appl. Phys. **83**, 3432 (1998).
[39] W. L. McMillan, Phys. Rev. **167**, 331 (1968).
[40] D. Singh, J. A. T. Barker, T. Arumugam, A. D. Hillier, D. M. Paul, and R. P. Singh, J. Phys.: Condens. Matter **30**, 075601 (2018).
[41] M. Isobe, M. Arai, and N. Shirakawa, Phys. Rev. B **93**, 054519 (2016).
[42] A. J. Drew, S. L. Lee, F. Y. Ogrin, D. Charalambous, N. Bancroft, D. M. Paul, T. Takabatake, and C. Baines, Physica B **374-375**, 270 (2006).
[43] M. Tinkham, *Introduction to Superconductivity*, 2nd ed. (Dover, Mineola, NY, 1996).
[44] Y. J. Uemura, V. J. Emery, A. R. Moodenbaugh, M. Suenaga, D. C. Johnston, A. J. Jacobson, J. T. Lewandowski, J. H. Brewer, R. F. Kiefl, S. R. Kreitzman, G. M. Luke, T. Riseman, C. E. Stronach, W. J. Kossler, J. R. Kempton, X. H. Yu, D. Opie, and H. E. Schone, Phys. Rev. B **38**, 909(R) (1988).
[45] Y. J. Uemura, G. M. Luke, B. J. Sternlieb, J. H. Brewer, J. F. Carolan, W. N. Hardy, R. Kadono, J. R. Kempton, R. F. Kiefl, S. R. Kreitzman, P. Mulhern, T. M. Riseman, D. Ll. Williams, B. X. Yang, S. Uchida, H. Takagi, J. Gopalakrishnan, A. W. Sleight, M. A. Subramanian, C. L. Chien, M. Z. Cieplak, Gang Xiao, V. Y. Lee, B. W. Statt, C. E. Stronach, W. J. Kossler, and X. H. Yu, Phys. Rev. Lett. **62**, 2317 (1989).
[46] Y. J. Uemura, L. P. Le, G. M. Luke, B. J. Sternlieb, W. D. Wu, J. H. Brewer, T. M. Riseman, C. L. Seaman, M. B. Maple, M. Ishikawa, D. G. Hinks, J. D. Jorgensen, G. Saito, and H. Yamochi, Phys. Rev. Lett. **66**, 2665 (1991).
[47] https://doi.org/10.5286/ISIS.E.67770571.